



HAL
open science

Validation of a mathematical model of arterial wall mechanics with drug induced vasoconstriction against ex vivo measurements

Sara Costa Faya, Wesley Callan, Marina Vidrascu, Miguel Angel Fernández, Pieter-Jan Guns, Damiano Lombardi

► To cite this version:

Sara Costa Faya, Wesley Callan, Marina Vidrascu, Miguel Angel Fernández, Pieter-Jan Guns, et al.. Validation of a mathematical model of arterial wall mechanics with drug induced vasoconstriction against ex vivo measurements. 2024. hal-04597238

HAL Id: hal-04597238

<https://inria.hal.science/hal-04597238>

Preprint submitted on 2 Jun 2024

HAL is a multi-disciplinary open access archive for the deposit and dissemination of scientific research documents, whether they are published or not. The documents may come from teaching and research institutions in France or abroad, or from public or private research centers.

L'archive ouverte pluridisciplinaire **HAL**, est destinée au dépôt et à la diffusion de documents scientifiques de niveau recherche, publiés ou non, émanant des établissements d'enseignement et de recherche français ou étrangers, des laboratoires publics ou privés.



Distributed under a Creative Commons Attribution 4.0 International License

Validation of a mathematical model of arterial wall
mechanics with drug induced vasoconstriction
against *ex vivo* measurements

Costa Faya Sara^{1*}, Wesley Callan², Vidrascu Marina¹,
Fernández Miguel A.¹, Guns Pieter-Jan², Lombardi Damiano¹

^{1*}Sorbonne Université & CNRS, UMR 7598 LJLL, 75005 Paris France –
Inria, 75012 Paris, France.

²University of Antwerp, 2000 Antwerp, Belgium.

*Corresponding author(s). E-mail(s): sara.costa-faya@inria.fr;
Contributing authors: callan.wesley@uantwerpen.be;
marina.vidrascu@inria.fr; miguel.fernandez@inria.fr;
pieter-jan.guns@uantwerpen.be; damiano.lombardi@inria.fr;

Abstract

In this work we investigate a mathematical model in order to reproduce experimental data of arterial compliance under the action of vasoconstrictors and vasodilators related to pharmacological studies. The considered model is a 3D-shell with active fibres. Model parameters are identified by means of an optimisation procedure. The resulting model was able to reproduce the experimental data and predict the system behaviour in scenarios other than those used for the parameter estimation. The results suggest that smooth muscle cells contraction modulates stiffness through direct fibre-induced regulation of vascular tone, while parameters related to the passive arterial wall component remain relatively stable across different vasoactive scenarios.

Keywords: Mathematical modelling, Parameter estimation Active fibres, 3D shell, Vascular smooth muscle cells, Validation against experimental data

1 Introduction

Arterial compliance, the capacity of the aorta to extend and recoil, is crucial for regulating cardiac output and maintaining blood flow in the systemic circulation (Thomas and Sumam, 2016). Conversely, arterial stiffness, the inverse of compliance, is a predictor of cardiovascular health (Shirwany and Zou, 2010; Vlachopoulos, 2010). Pulse wave velocity (PWV) serves as a non-invasive method to evaluate arterial stiffness in both human and animal subjects, indicating the speed of propagation of blood pressure waves (Ghosh et al, 2019; Wang et al, 2016). PWV measurement can provide a comprehensive assessment of arterial stiffness either globally, using applanation tonometry (Sahani et al, 2016; Zhang et al, 2014), or locally, via ultrasound imaging (Vlachopoulos, 2010; Sharif et al, 2019). During ageing, PWV increases due to arterial remodelling in response to prolonged haemodynamic stress, reflecting changes in the extracellular matrix such as the elastin: collagen ratio, which affects structural wall stiffness (Shirwany and Zou, 2010; De Moudt et al, 2022b).

Traditionally, arterial stiffness was attributed solely to the passive biomechanical properties of the aorta (Leloup et al, 2016). However, recent investigations have underscored the dynamic involvement of vascular smooth muscle cells (SMCs) and endothelial cells (ECs) in regulating arterial stiffness through modulation of vascular tone (Kerage et al, 2014; Sehgel et al, 2013). This active stiffness modulation, facilitated by adjustments in vascular tone, enables adaptation to acute hemodynamic stress through vasoconstriction by SMCs and release of vasoactive molecules by ECs (Lacolley et al, 2017). While PWV is an independent predictor of cardiovascular health, it lacks the ability to provide detailed insights into passive or active modifications of arterial stiffness (Leloup et al, 2016, 2019). To address this, arterial stiffness can be studied in dedicated *ex vivo* setups, offering the advantage of isolating passive stiffness and evaluating active modulation independent of *in vivo* factors, such as heart rate or blood pressure (De Moudt et al, 2022b; Leloup et al, 2016, 2019). Previously,

our Rodent Oscillatory Tension Setup for measuring Arterial Compliance (ROTSAC) effectively distinguished between active and passive contributions to arterial stiffness (Leloup et al, 2016, 2019). Interestingly, we previously demonstrated that vasoconstrictors increased active stiffness at lower pressures while simultaneously reducing overall stiffness at higher pressures (Leloup et al, 2019; De Moudt et al, 2022a).

The present work is aimed to develop a mathematical model that most accurately recapitulates the pressure-diameter relationship of the elastic modulus¹ E_p , which is adjusted for diameter dependency. This investigation is essential for understanding mechanical behaviour of the aorta under varying pressure conditions. We aimed to establish a model capable of simulating the active contribution of SMCs to arterial stiffness. The objective of this work is twofold: firstly, our model has been designed with the purpose of reproducing the available experimental data of the setup proposed in Leloup et al (2016). Secondly, we aim to get insight whether SMCs contraction modulates stiffness through a direct fibre-induced regulation of vascular tone (*scenario I*) and, additionally, also through indirect adjustment of intrinsic stiffness (reflected by the Young modulus E) (*scenario II*), and to what extent changes in geometry (i.e., diameter) are modulating biomechanical assessment. A specific question was whether the *in silico* model could reflect the collagen unloading phenomena at elevated pressures that we previously reported (Leloup et al, 2019; De Moudt et al, 2022a).

The paper is organised as follows: Section 2 provides details on the experimental setup and discusses the available data for the simulations. It also presents the mathematical model considered to model the arterial wall with active behaviour. Section 3 showcases some of the numerical results. Section 4 presents the conclusions and future work of this study.

¹ E_p is the Peterson modulus of elasticity and will be defined in the next section.

2 Methods

In this section, the experimental methods and the collected data (see Appendix A for more details) that have been employed for the numerical simulations are presented. It also provides an overview of the structural model that has been used to reproduce the experimental data and to give some insight of the fore-mentioned scenarios. Finally, this section introduces the methodology employed for parameter estimation and model validation.

2.1 Experimental data

Evaluation of vascular reactivity

For the evaluation of vascular reactivity, aortic segments were set at a preload of 20 mN to achieve a mean pressure of 100 mmHg. SMC contraction was assessed by incremental concentrations of phenylephrine (PE; ranging from 3 nM to 3 μ M), an α 1-adrenergic receptor agonist. Subsequently, endothelium-dependent relaxations were evaluated by cumulative concentrations of acetylcholine (ACh; ranging from 3 nM to 10 μ M), a muscarinic receptor agonist. To mitigate the influence of nitric oxide (NO), L-Nitro arginine methyl ester (L-NAME; 300 μ M), a non-selective NO synthase inhibitor, was administered. Furthermore, exogenous nitric oxide donor, 2-(N,N-diethylamino)-diazonolate-2-oxide sodium salt hydrate (DEANO; ranging from 0.03 nM to 10 μ M) was administered to investigate endothelium-independent SMC relaxation.

Ex vivo stiffness

The *ex vivo* stiffness of aortic segments was assessed using the Rodent Oscillatory Setup to study Arterial Compliance (ROTSAC), as detailed by [Leloup et al \(2016\)](#) (see Figure 1(left)). Briefly, 2 mm aortic segments were placed between two parallel hooks within 10 mL organ baths. These segments were submerged in Krebs-Ringer (KR) solution maintained at 37 °C, with a gas mixture of 95% O₂ and 5% CO₂, and pH

adjusted to 7.4. The composition of the Krebs-Ringer solution comprised NaCl 118 mM, KCl 4.7 mM, CaCl₂ 2.5 mM, KH₂PO₄ 1.2 mM, MgSO₄ 1.2 mM, NaHCO₃ 25 mM, CaEDTA 0.025 mM, and glucose 11.1 mM. Force and displacement of the upper hooks were controlled and recorded using a force length transducer. Aortic segments underwent cyclic stretching between alternating preloads, mimicking “diastolic” and “systolic” transmural pressures at a frequency of 10 Hz, corresponding to the physiological heart rate in mice (600 beats per minute). Transmural pressure was determined using the Laplace relationship. Aortic extension was calibrated through optical camera imaging, capturing pictures at different stretches to calibrate the upper hook and allowing calculation of vessel diameters during systole and diastole. Subsequently, the Peterson modulus of elasticity, E_p , was computed at various pressure levels. E_p was calculated using the formula:

$$E_p = D_0 \frac{\Delta P}{\Delta D},$$

where ΔP represents the difference in pressure (maintained constant at 40 mmHg), D_0 denotes the “diastolic” diameter, and ΔD indicates the change in diameter between “diastolic” and “systolic” pressure. The protocol encompassed the assessment of arterial stiffness (E_p) at different pressures, ranging from 60 – 100 mmHg up to 120 - 160 mmHg, with incremental intervals of 20 mmHg. The pressure-stiffness relationship was evaluated under physiological conditions (using Krebs-Ringer solution), in a maximally-contracted state (induced by 2 μ M PE, serotonin (5HT) or potassium (50K) reflecting active components), and in the absence of active stiffness (utilising 2 μ M of DEANO, a nitric oxide donor to negate any contribution of SMC contraction).

2.2 Mathematical modelling

Arteries form an anisotropic structure composed of three primary layers (for more details, please refer to [Bit et al \(2020\)](#)): the adventitia, situated on the outermost part, contains collagen fibres and acts as a protective covering for the artery; below the

adventitia lies the media layer, housing SMCs that are responsible for vascular tone regulation; and the innermost intima, lined with ECs, serves as a protective barrier between the bloodstream and arterial wall.

In the present work, the arterial wall is modelled as a passive hyperelastic material using a 3D-shell model. Additionally, a layer of fibres is included to describe the SMCs induced vasoconstriction and vasodilation phenomena. Since the focus is primarily on the media layer, the fibres are aligned with the vertical direction (Murtada and Holzapfel, 2014). The anisotropic behaviour of the passive matrix due to collagen fibres is neglected.

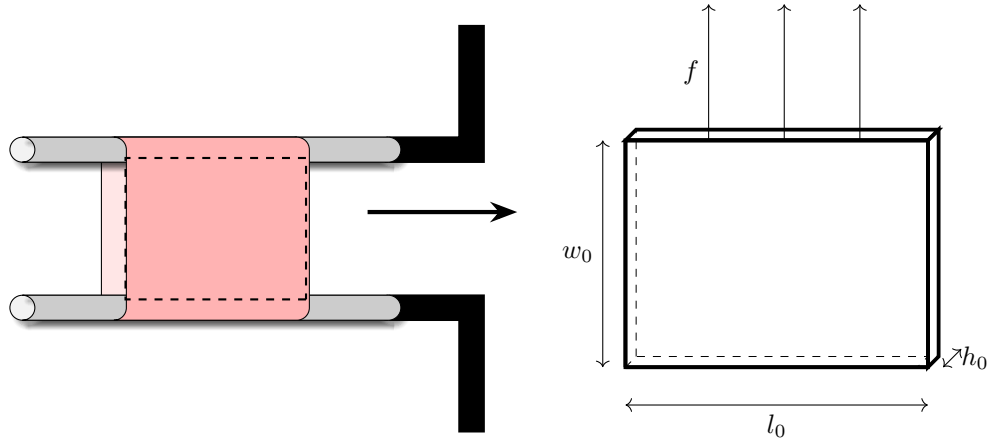


Fig. 1: ROTSAC setup (left) and simplified geometry considered in the mathematical model (right)

Owing to the symmetry of the ROTSAC setup (Figure 1(left)), a simplified geometrical configuration has been considered in the mathematical model. It consists of one of the lateral sides of the tissue mounted on the hooks, as presented in Figure 1(right), which is here assumed to be flat in the stress free configuration.

2.2.1 3D-shell model

Let $\Omega \subset \mathbb{R}^3$ denote the reference (stress free) configuration of the tissue segment. The boundary of $\partial\Omega$ is partitioned into three subsets: Γ_N , which corresponds to the upper boundary of the domain where the force is applied to stretch the tissue; Γ_D , representing the part of the aortic segment attached to the lower hook, which is clamped during the whole experiment; and Γ_L , that are the lateral boundaries of the aortic segment. We denote by \mathbf{n} the outward unit normal on the boundary Γ_N . The reference configuration Ω is characterised by l_0 , w_0 and h_0 , that are the stress free length, width and thickness, respectively, as shown in Figures 1(right) and 2.

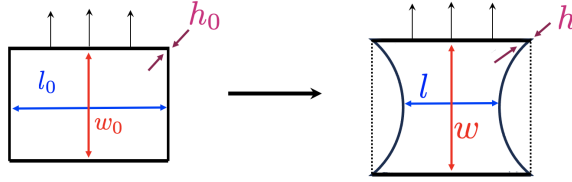


Fig. 2: Geometrical configuration of the shell. On the left the reference configuration and on the right the deformed one

The deformation of the continuum medium is given as the map $\varphi : \Omega \times [0, T] \mapsto \mathbb{R}^3$. The deformation gradient \mathbf{F} , is expressed as $\mathbf{F}(\mathbf{x}, t) = \nabla_{\mathbf{x}}\varphi(\mathbf{x}, t)$, and its determinant J , as $J(\mathbf{x}, t) = \det(\mathbf{F}(\mathbf{x}, t))$. The displacement field \mathbf{d} is defined as $\mathbf{d}(\mathbf{x}, t) = \varphi(\mathbf{x}, t) - \mathbf{x}$.

The equilibrium of the system is given by the following non-linear elastodynamics boundary value problem:

$$\left\{ \begin{array}{ll} \rho \partial_{tt} \mathbf{d} - \operatorname{div}(\mathbf{F}(\mathbf{d})\boldsymbol{\Sigma}(\mathbf{d})) = \mathbf{0}, & \text{in } \Omega, \\ \mathbf{F}(\mathbf{d})\boldsymbol{\Sigma}(\mathbf{d})\mathbf{n} = \mathbf{f}_s, & \text{on } \Gamma_N, \\ \mathbf{d} = \mathbf{0}, & \text{on } \Gamma_D, \end{array} \right. \quad (1)$$

where ρ stands for the density of the tissue, \mathbf{f}_s represents the time-dependent pulling force and $\boldsymbol{\Sigma}(\mathbf{d})$ the (second Piola-Kirchhoff) stress tensor of the tissue.

The active SMC fibres are assumed to be perfectly attached to the solid so that to model the active behavior of the artery wall, an active-stress formalism (Ambrosi and Pezzuto, 2012) is chosen, which consists in adding an active component to the passive stress tensor (Decoene et al, 2023), viz.,

$$\boldsymbol{\Sigma}(\mathbf{d}) = \boldsymbol{\Sigma}_p(\mathbf{d}) + \boldsymbol{\Sigma}_a(\mathbf{d}),$$

with $\boldsymbol{\Sigma}_a(\mathbf{d})$ and $\boldsymbol{\Sigma}_p(\mathbf{d})$ respectively denoting the active and passive components of the stress.

An Ogden hyperelastic constitutive law is chosen to describe the homogeneous and isotropic passive component, since it accommodates large deformations and non-linear material responses, providing a more accurate representation for the behaviour of complex materials like biological tissue (Lohr et al, 2022; Nedrelov et al, 2023). We hence have

$$\boldsymbol{\Sigma}_p = \frac{\partial W}{\partial \mathbf{C}},$$

where $\mathbf{C} = \mathbf{F}^T \cdot \mathbf{F}$ stands for the right Cauchy-Green deformation tensor and the strain energy density function W given by the relation (Geymonat and Ciarlet, 1982):

$$W = c_1(I_1 - 3) + c_2(I_2 - 3) + a(I_3 - 1) - (c_1 + 2c_2 + a)\ln(I_3), \quad (2)$$

in terms of the invariants of \mathbf{C} , namely, $I_1 = \text{tr}(\mathbf{C})$, $I_2 = \frac{1}{2}(I_1^2 - \mathbf{C} \cdot \mathbf{C})$, and $I_3 = \det(\mathbf{C}) = J^2$.

In (2), the constants c_1 , c_2 and a stands for the material parameters, that can be expressed as a function of the Young modulus, E , and the Poisson ratio, ν , as follows

(see Appendix B):

$$\begin{cases} c_1 = \frac{E}{4(1+\nu)(1+\frac{1}{\kappa})}, \\ c_2 = \frac{c_1}{\kappa}, \\ a = \frac{\nu E}{4(1+\nu)(1-2\nu)} - \frac{c_1}{\kappa}, \end{cases}$$

where usually c_2 can be chosen such that $c_2 = c_1/\kappa$, with $\kappa \in [2, 100]$.

The elastodynamics equations (1) can be reformulated in weak variational form as follows

$$\begin{cases} \text{Find } \mathbf{d} \in \mathbf{V} \text{ such that} \\ \int_{\Omega} \rho \partial_{tt} \mathbf{d} \cdot \mathbf{v} + \int_{\Omega} \boldsymbol{\Pi}(\mathbf{d}) : \nabla \mathbf{v} = \int_{\Gamma_N} \mathbf{f}_s \cdot \mathbf{v}, \quad \forall \mathbf{v} \in \mathbf{V}, \end{cases} \quad (3)$$

where \mathbf{V} is the space of admissible displacements.

The numerical approximation of (3) is performed via the finite element method, in which the space \mathbf{V} is replaced by the discrete space $\mathbf{V}_{\mathcal{H}}$. In this paper, this space is made of 3D-shell elements which have quadratic displacements across the thickness and affine on each section (Chapelle et al, 2004; Libai and Simmonds, 2005; Chapelle and Bathe, 2010). This yields a $\mathbb{P}_1 \otimes \mathbb{P}_2$ prism element with 9 nodes (see Figure 3). Numerical locking is avoided using a MITC (Mixed Interpolated Tensorial Components) approach. This approach guarantees robustness while including the effects of the through-the-thickness normal stress and can be employed with general constitutive laws.

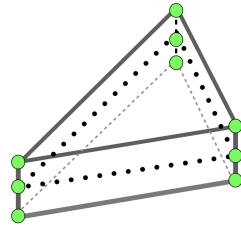


Fig. 3: $\mathbb{P}_1 \otimes \mathbb{P}_2$ 3D-shell element

All the simulations presented in this work have been performed using FELiScE¹.

2.2.2 Active fibre model

The main hypotheses regarding the fibres are the following:

- The fibres are part of the shell and are distributed through the thickness in the vertical direction;
- There is no sliding between the fibres and the shell;
- The fibres are characterised by an affine stress-strain constitutive law.

Here, we consider the active fibres model proposed in [Aletti et al \(2015\)](#), so that

$$\boldsymbol{\Sigma}_a = (k_0 + k_1 e_{\mathbf{ff}}) \mathbf{f} \otimes \mathbf{f}, \quad (4)$$

where k_0 denotes the pre-stress of the fibre, k_1 is the elastic modulus, $e_{\mathbf{ff}}$ is the fibre deformation and \mathbf{f} is the unitary tangent vector to the fibre direction. The deformation along the fibre directions is given by the relation $e_{\mathbf{ff}} = \mathbf{f}^T \mathbf{e} \mathbf{f}$, where \mathbf{e} is the Green-Lagrange strain tensor (defined in equation (C2) in Appendix C).

2.3 Parameter estimation and model validation

The mathematical model (3), together with the hyperelastic law (2) and the fibres constitutive law (4), contains a set of parameters (Young modulus, E ; active pre-stress, k_0 , and elastic modulus, k_1 , of the fibres; κ , that stems from the Ogden's law; initial length, l_0 , width, w_0 , and thickness, h_0 , of the aortic segment) that are unknown and are determined through a parameter estimation procedure. After spatial and temporal discretisation, the model (3), with (2) and (4), yield the non-linear system

$$F(\mathbf{f}_s, \boldsymbol{\theta}; \mathbf{Y}) = 0, \quad (5)$$

¹<https://gitlab.inria.fr/felisce>

where \mathbf{f}_s is the given force, that can be measured, $\boldsymbol{\theta} = (E, k_0, k_1, \kappa; l_0, w_0, h_0)$ are the model parameters and \mathbf{Y} is the model output, that corresponds to the displacement degrees of freedom. The inputs of the model are $\boldsymbol{\theta}$ and \mathbf{f}_s .

The purpose of the parameter estimation is evaluating some unknown inputs of the model such that the outputs match the experimental measurements. The parameter estimation problem can be formulated as follows: given the force \mathbf{f}_s , the discrete model (5) and the experimental data, find the parameters $\boldsymbol{\theta}$ that minimise the discrepancy between the simulated model predictions and measurements. Mathematically, this problem can be formulated as the optimisation problem

$$\min_{\substack{\boldsymbol{\theta} \in \mathbf{W} \\ F(\mathbf{f}_s, \boldsymbol{\theta}, \mathbf{Y})=0}} J(\mathbf{Y}), \quad (6)$$

where $J : \mathbb{R}^n \rightarrow \mathbb{R}$ is given cost function (viz., discrepancy between simulation and measurements) and $\mathbf{W} \subset \mathbb{R}^n$ stands for the set of admissible parameters. In this paper, problem (6) is solved via a Control Random Research (CRS) optimisation algorithm (see Appendix E).

Initially, the estimation is done for each aortic segment under Krebs-Ringer solution. Subsequently, estimations are conducted after the introduction of a vasoactive drug, either a vasoconstrictor or vasodilator. The results of the parameter estimation provides hence insight on whether the compound solely impacts SMCs (scenario I) or additionally introduces additional intrinsic stiffness (scenario II). Specifically, if only the fibre parameters from the active contribution, such as k_0 and k_1 , are affected, it suggests that the first scenario is the most plausible one. However, if the Young's modulus also needs modification, then the compound is likely to introduce stiffness (scenario II). To establish a range for the active pre-stress parameter, data from isometric experiments have been used.

To solve the optimisation problem (6), a CRS2 with local mutation optimisation algorithm (Kaelo and Ali, 2006) (for more details, see appendix E) that is implemented in the NLOpt non-linear optimisation package by Johnson (2014) has been employed.

2.3.1 Parameter estimation in baseline conditions

During the ROTSAC static calibration, the experimental measurements are the length (l_m) and the width (w_m) of the aortic segments for some given forces \mathbf{f}_s while when the segments are dynamically stretched, the measured data is the width (\tilde{w}_m). In this case, the cost function of the parameter estimation problem (6) has the following form

$$J_1(\mathbf{Y}) = \frac{1}{k} \sqrt{\sum_{i=1}^k \left| l^{(i)}(\mathbf{Y}) - l_m^{(i)} \right|^2 + \left| w^{(i)}(\mathbf{Y}) - w_m^{(i)} \right|^2} + \frac{1}{n} \sqrt{\sum_{i=1}^n \left| \tilde{w}^{(i)}(\mathbf{Y}) - \tilde{w}_m^{(i)} \right|^2}. \quad (7)$$

Here, $l_m^{(i)}$ and $w_m^{(i)}$ represent the measured length and width, respectively, during static experimental calibration, with $i = 1, \dots, k$ denoting the number of measurements. $\tilde{w}_m^{(i)}$ denotes the measured width during oscillation, with $i = 1, \dots, n$ indicating the number of measurements. $l^{(i)}(\mathbf{Y})$ and $w^{(i)}(\mathbf{Y})$ represent the predicted values of length and width, respectively, during static experimental calibration, while $\tilde{w}^{(i)}(\mathbf{Y})$ denotes the predicted value of width during the oscillation.

2.3.2 Parameter estimation in the presence of vasoactive substances

Determination of the range of the pre-stress

The isometric experiments provide data that show the force exerted by the vessel in response to a specific vasoconstrictor (or vasodilator) dosage within a static setup. The relevance of these experiments, is that they can provide an estimation of the range of the value of the active pre-stress at each drug concentration C , with C being either C^{PE} , the PE concentration, or C^{DEANO} , the DEANO concentration. In particular,

the ROTsAC measurements were taken at $C = 2 \mu\text{M}$ and the isometric data allow the estimation of the range of the value of k_0 at the specified C .

We consider that the total measured force is

$$F_m = \beta + F_1, \quad (8)$$

where β is the force at zero concentration and F_1 is the isometric force felt by the upper hook in the presence of a vasoactive substance. Assume that the relation between F_1 and the active pre-stress, k_0 , is linear and can be expressed as $F_1 = \alpha k_0$. The mathematical model (3)–(4), has been used applying homogeneous Dirichlet boundary conditions on the upper and on the lower boundary of the domain Ω to estimate α . Substituting the expression for F_1 in (8), $F_m = \beta + \alpha k_0$.

Using the following tension-dose relationship (Yosibash and Priel, 2012), the active pre-stress results

$$k_0(C; m, EC_{50}) = S_{\max}^{\text{PE}} \frac{[C^{\text{PE}}]^m}{[C^{\text{PE}}]^m + EC_{50}^m} - S_{\max}^{\text{DEANO}} \frac{[C^{\text{DEANO}}]^m}{[C^{\text{DEANO}}]^m + EC_{50}^m}, \quad (9)$$

where S_{\max}^{PE} is the maximal tension for PE (saturation level), S_{\max}^{DEANO} is the maximal tension for DEANO, m is the slope parameter and EC_{50} the concentration at which 50% of maximal force is obtained.

Finally, the expression of the total measured force is

$$F_m = \beta + \alpha \left(S_{\max}^{\text{PE}} \frac{[C^{\text{PE}}]^m}{[C^{\text{PE}}]^m + EC_{50}^m} - S_{\max}^{\text{DEANO}} \frac{[C^{\text{DEANO}}]^m}{[C^{\text{DEANO}}]^m + EC_{50}^m} \right). \quad (10)$$

During the isometric experiments, the aortic segments have been preloaded with a force $\beta = 20 \text{ mN}$ in the absence of drugs ($C^{\text{PE}} = C^{\text{DEANO}} = 0$) and also S_{\max}^{PE} and S_{\max}^{DEANO} are known. By employing the previous F_m - dose relation, a fitting of the

measured forces to equation (10) to estimate the values of m and EC_{50} was performed. After fitting the measured force for several concentrations in the set of aortic segments, it is possible to determine the range of k_0 for a vasodilator or for a vasoconstrictor.

From equation (9), it can be remarked that when there is only PE in the organ bath, $C^{\text{DEANO}} = 0$ and the second term vanishes. After DEANO has been added on the bath, C^{PE} is equal to the concentration at saturation, so $C^{\text{PE}} = 3 \mu\text{M}$.

Dynamic oscillation

In the context of ROTSAC dynamic oscillation with vasoconstrictors/vasodilators, two scenarios are tested. In the first one, only the active fibre parameters k_0 and k_1 are subject to estimation, while E , l_0 , w_0 , and h_0 remain fixed based on the corresponding segment in Krebs-Ringer solution. Conversely, in the second scenario, parameters E , k_0 , k_1 , and h_0 are open to estimation, with l_0 and w_0 held constant. The key distinction lies in allowing E to vary during estimation for the second scenario, whereas only the active fibre parameters are adjusted in the first one. Here the parameter estimation is done when a vasoconstrictor (PE, 5HT, or 50K) or a vasodilator (DEANO) are added to the Krebs-Ringer solution to assess the effects. The available experimental measurements are the values of width (\tilde{w}_m) of the aortic segment dynamically stretched at 80-120 mmHg. Under the effect of a drug, the cost function of the minimisation problem (6) is

$$J_2(\mathbf{Y}) = \sqrt{\sum_{i=1}^n \left| \tilde{w}^{(i)}(\mathbf{Y}) - \tilde{w}_m^{(i)} \right|^2}, \quad (11)$$

where $\tilde{w}_m^{(i)}$ is the measured experimental value of the width and $\tilde{w}^{(i)}(\mathbf{Y})$ is the predicted value of the width at each point $i = 1, \dots, n$ during the oscillation. Since there are not static experimental calibration data with drugs, there is not information of the length in the case of a vasoactive substance on the organ bath. The changes in the fibre parameters k_0, k_1 and in E, h_0 , will help to assess the fore-mentioned scenarios.

3 Results

First, the results that arise from the parameter estimation of the model are presented. Next, numerical simulation (in baseline conditions and in the presence of vasoactive compounds) is performed. While various vasoconstrictors have been employed, the outcomes will be primarily focused on PE due to its resemblance to the others. Finally, the behaviour of the aortic segments under varying pressure conditions is explored.

3.1 Static experimental calibration

The static experimental calibration measurements of the length and width at different preloads (10, 20, 30, 40, 50, and 60 mN) were considered for estimating the parameters θ of each aortic segment in the baseline case (Krebs-Ringer solution), together with the dynamic data at 80 - 120 mmHg (using the cost function (7) with $k = 5$ and $n = 80$). The static part of results for the set of fifteen aortic segments considered in this study are shown in Figure 4.

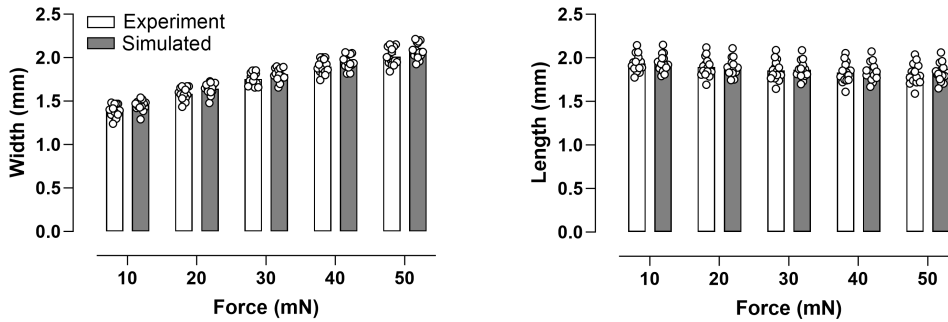


Fig. 4: Comparison between experimental and simulated static experimental calibrations

3.2 Simulation in the presence of vasoactive substances

Estimation of the range of the pre-stress from the isometric data

First, throughout the isometric tests, where a second set of nine aortic segments was considered, the average relative mean squared error (RMSE) between the experimental and simulated data across all fittings of the isometric force (10) in the presence of PE ($2 \mu\text{M}$) is $0.56\% \pm 0.38\%$, while $1.86\% \pm 0.63\%$ for DEANO, ($2 \mu\text{M}$) (see the fittings in Figure D1 in Appendix D). The results at $C = 2 \mu\text{M}$ – the concentration at which dynamic measurements were taken – are shown in Figure 5. Upon examination of the values of the pre-stress, k_0 , for the available set of aortic segments at a concentration of $C = 2 \mu\text{M}$, the range of k_0 for PE and DEANO can be identified (see Figure 5). The observed range of k_0 was $[0.023, 0.067]$ MPa for PE and $[-0.00014, 0.0043]$ MPa for DEANO. The fitting for all the concentrations is presented in in Figure D2 in Appendix D.

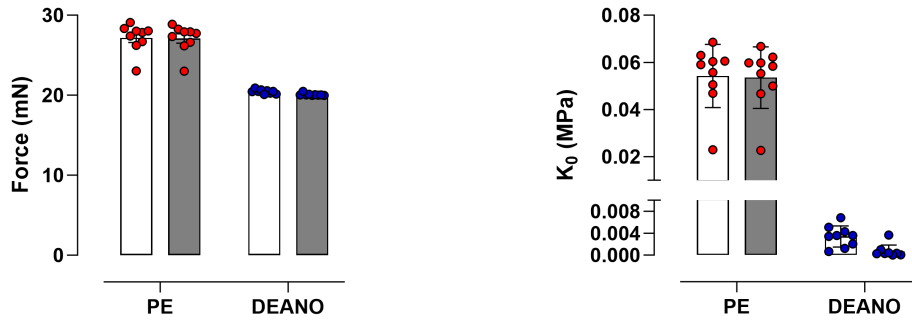


Fig. 5: Isometric force F_m at $C = 2 \mu\text{M}$ (left); pre-stress at $C = 2 \mu\text{M}$ (right)

Simulation of ROTSAC dynamic oscillation data

Next, parameters were estimated and numerical simulations of experimental data were conducted across 15 segments using a Krebs-Ringer solution (using the cost function (7)). From the set of all segments, Table 1 details the estimated parameters

for one aortic segment (seg #1) under baseline, contracted, and dilated conditions, with corresponding experimental and simulated datasets shown in Figures 6A and 6B. Figure 6 illustrates the impact of vasoconstrictors and vasodilators on arterial behaviour (with the parameter estimation performed using the cost function (11) with $n = 80$). Particularly, Figure 6C displays the Peterson modulus derived from experimental and simulated data under KR, PE, and DEANO conditions, while aortic segments underwent oscillations within the pressure range of 80 - 120 mmHg. This graphical representation highlights differences in stiffness across these conditions, with PE exhibiting heightened stiffness relative to baseline, and DEANO resulting in comparable stiffness to baseline. Such observations underscore the model’s adeptness in capturing the vascular system’s mechanical responses to various vasoactive agents.

Table 1: Parameters and stress-free configuration for KR, PE, and DEANO for seg #1 in scenario II for PE and DEANO

Parameter	KR	PE	DEANO
E (MPa)	0.13248	0.13248	0.12717
k_0 (MPa)	$6.4 \cdot 10^{-6}$	0.01	$-1.348 \cdot 10^{-4}$
k_1 (MPa)	0.191	0.457	0.188
	l_0 (mm) = 1.97	w_0 (mm) = 0.13	h_0 (μ m) = 53

Correlation plots (Figures 6D, 6E, 6F) were generated to measure the concordance between simulated and experimental data across different conditions. A statistical covariance matrix $Q \in \mathbb{R}^{2 \times N}$ was computed to quantify variability and correlation, with $N \in \mathbb{N}$ representing the number of points. From Q , a matrix $C = \frac{1}{N-1} Q Q^T \in \mathbb{R}^{2 \times 2}$ was derived to reveal the shape and orientation of ellipses. The eigenvectors of C represent the principal axes of the ellipse and the square root of its eigenvalues will determine the ellipse’s width and height, with one of them reflecting the average difference between simulated and experimental data (RMSE) and another one giving an idea of the standard deviation of the fits. Overall, the correlation plots demonstrate a

consistent match between the simulated and experimental data, indicating the model's capability in capturing the SMCs behaviour under KR, PE, and DEANO.

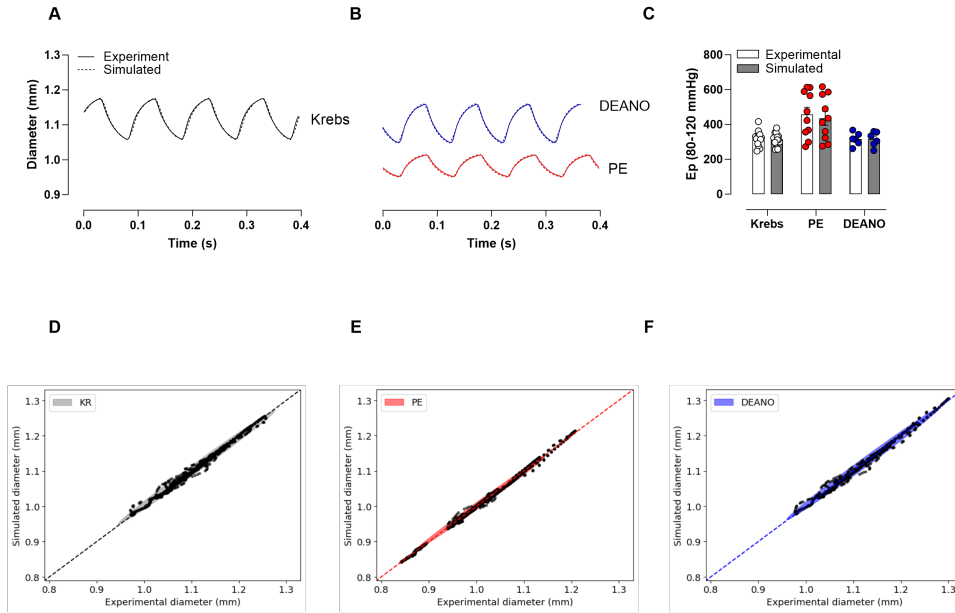


Fig. 6: Analysis of the impact of PE and DEANO when the segments are dynamically stretched at 80 - 120 mmHg. Time evolution of the experimental and simulated diameters of seg #1 (A,B); Peterson modulus (C); Correlation between experimental and simulated diameters (D,E,F). The ellipse intersects the unity line, which depicts where the simulated and experimental data would coincide perfectly, being the center of the ellipse the average position of the points

Assessing the role of SMCs

Finally, comparisons between the changes of fibre parameters (k_0 and k_1) in the presence of a vasoconstrictor or vasodilator with E and h_0 constant (scenario I) or with re-estimation of E and h_0 (scenario II) were investigated. The analysis depicted in Table 2 illustrates the effectiveness of integrating k_0 and k_1 under constant E and h_0 conditions to fit dynamical experimental data within the pressure range of 80 - 120 mmHg.

Table 2: Average of the RMSE of the dynamic fittings for Krebs-Ringer and in both scenarios (Scn1 or Scn2) at 80 - 120 mmHg

KR (%)	Scn1 PE (%)	Scn2 PE (%)	Scn1 DEANO (%)	Scn2 DEANO (%)
0.60	1.60	0.44	0.63	0.58

The mean of the RMSE for fittings indicates an overall relative error of less than 2%, suggesting that the compound primarily impacts the SMCs. However, in cases where the error is larger, it may indicate that the compound also affects the intrinsic stiffness of the vessel, necessitating adjustments to parameters such as the Young modulus or thickness. Overall, the results suggest that the change of k_0 and k_1 in the presence of a vasoconstrictor or vasodilator with E and h_0 constant, is generally sufficient, but there might be cases where improvements can be made by re-estimating E and h_0 .

The active fibre parameters were changed in the presence of a vasoconstrictor with respect to the baseline (Figures 7A and 7B). The pre-stress is also seen to increase with the introduction of a vasoconstrictor (Figure 7A, $p < 0.01$). The active elastic modulus experienced an increase (Figure 7B, $p < 0.01$), indicating an augmentation in vessel stiffness. No differences were reported in the change in Young modulus following constriction with PE (Figure 7C). Overall, the majority of segments underwent a Young modulus change within the range of $[-1, 1]$ %. While some cases exhibited a slightly larger deviation, on the whole, the scenario in which the change of fibre parameters (k_0 and k_1) in the presence of a vasoconstrictor or vasodilator with E and h_0 constant appears to be a plausible one. No changes in aortic thickness were reported following PE stimulation (Figure 7D).

For simplicity, the results for DEANO were excluded from the graphs as they closely resemble those of KR. However, the response to DEANO is more complex to interpret, where the pre-stress may either rise or fall relative to the baseline. It's important to acknowledge that DEANO was administered alongside the vasoconstrictor in

the organ bath, making it challenging to isolate its specific effect. Among vasodilators, changes in pre-stress exhibit diverse patterns—sometimes increasing, other times decreasing. Vasodilators typically lower blood pressure and wall tension by dilating vessels and enhancing compliance, resulting in an overall reduction in pre-stress. However, the complex interaction of compensatory mechanisms and individual variations can influence the effect on pre-stress. On the other hand, with the other parameters (k_1 , E and h_0) the obtained results are very close to the ones of KR.

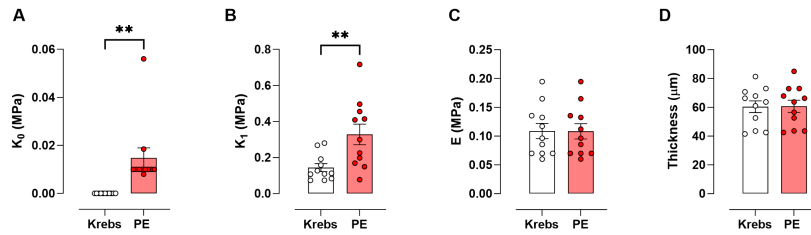


Fig. 7: Vessel parameters under different conditions. Change of the pre-stress (A), fibres elastic modulus (B), Young modulus (C) and thickness (D) for PE with respect to the baseline. The values for a vasodilator (DEANO) are omitted since they are very similar to the ones of KR

Evaluating the model in different pressure ranges

After presenting the estimated parameters for each scenario, additional model validation was conducted by examining the predictability across different pressure ranges. The outcomes corresponding to the segment with parameters outlined in Table 1 (seg #1) are illustrated in Figure 8. The oscillations were represented only for KR and PE since the ones for DEANO are very similar to the ones of KR.

When aortic segments were stretched in Krebs-Ringer solution, the original estimated parameters were able to reproduce the data both in the ranges of 60 - 100 mmHg to 100 - 140 mmHg. However, there was an underestimation at higher pressures

(120 - 160 mmHg). One possible explanation could be because the segments exhibited plasticity and they did not recover the reference configuration (l_0 , w_0 and h_0) instantaneously. Consequently, it was necessary to take into account that the reference configuration had changed after large forces were applied. Then, a re-estimation of l_0 , w_0 and h_0 was needed for the pressure range 120 - 160 mmHg, while the rest of the parameters (E , k_0 and k_1) were kept constant. After PE was added to the Krebs-Ringer solution, the change of the reference configuration was observed in all the pressure ranges so, again, the re-estimation of the initial length, width, and thickness was necessary. Finally, once DEANO was added to the organ bath, a similar behaviour was observed, so the re-estimation was only needed for the highest pressure range.

From a biological perspective, the underestimation at higher pressures can be attributed to the properties of the arterial wall. When subjected to elevated forces, such as those experienced at higher pressure ranges, arterial segments may encounter layers of collagen within their structure. This discrepancy is particularly pronounced in KR solution, where the arterial segments experience greater pressure-induced deformation. Conversely, when PE is added, the effects are mitigated to some extent. This is because PE-induced constriction leads to smaller diameter arteries, reducing the likelihood of encountering collagen layers and thus minimising the bouncing effect.

From a mathematical point of view, the underestimation arises from a different perspective. Rather than adjusting the stiffness of the model, which remains constant, the observed phenomenon can be explained by changes in the reference configuration of the arterial segments. When subjected to higher pressures, the segments exhibit plasticity and fail to immediately return to their original reference configuration (l_0 , w_0 , and h_0). This deviation from the reference configuration needs a (re)estimation of these parameters to capture the behaviour of the arterial segments under the new pressure conditions. In summary, while from a biological perspective the focus is on altering stiffness to explain the observed phenomena, from a mathematical one, the

adjustment of the configuration parameters to account for the changes in arterial behaviour is done.

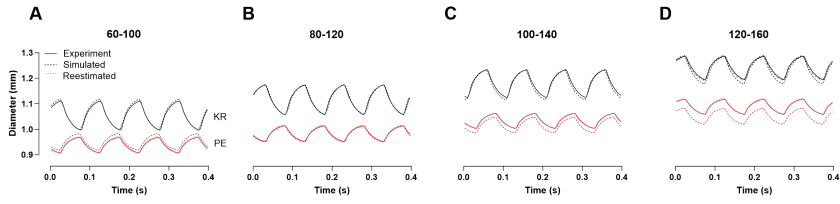


Fig. 8: Pressure steps under Krebs-Ringer and PE of one aortic segment

The active pressure-stiffness curve (Figure 9B) demonstrates elevated arterial stiffness levels at lower mean pressures (80, 100 mmHg) in contrast to those observed under KR (Figure 9A) and DEANO (Figure 9C) conditions. This distinction is further evident in the corresponding diameter measurements, where exposure to PE (Figure 9E) yielded smaller diameters relative to those observed under KR (Figure 9D) and DEANO (Figure 9F) conditions. Consequently, this phenomenon leads to an augmented arterial stiffness, indicative of an enhanced buffering capacity and concomitant elevation in vascular tone. However, as mean pressures increase, the recruitment of collagen emerges as the predominant load-bearing component within the aortic wall. The absence of stiffer collagen fibres within our current model results in an underestimation of stiffness values at highest pressure (Figure 9A, 9B, 9C).

4 Discussion

In this study, we set up a mathematical framework capable of capturing both vasoconstriction and vasodilation, facilitating the comprehension of the mechanical behaviour of arterial segments and the role of SMCs in arterial stiffness. This model was calibrated using isometric data to simulate the action of molecules on SMCs. Importantly, we not only established the model but also validated it against experimental data and

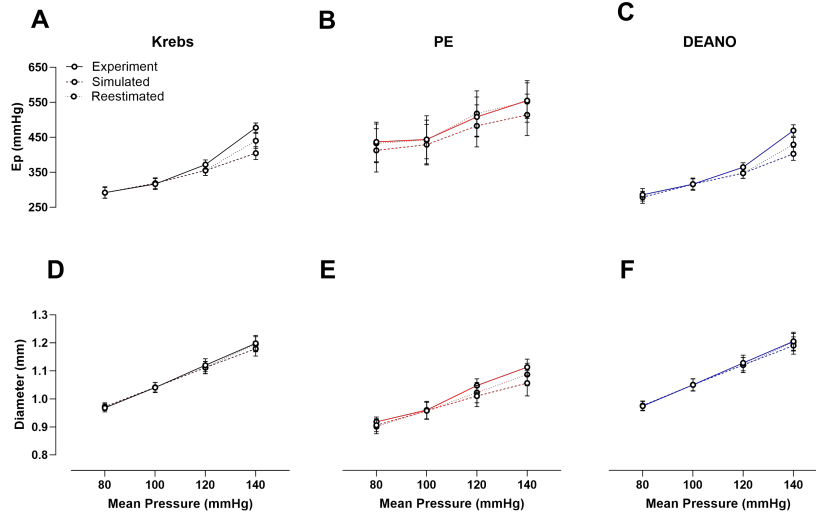


Fig. 9: Diastolic diameter and Peterson modulus for KR, PE and DEANO under different pressure steps

explored two distinct scenarios to evaluate the impact of the active contribution of SMCs on arterial mechanics. Furthermore, the model was tested with different pressure conditions beyond those used for parameter estimation, demonstrating its capacity of representing the pressure-diameter relationship except some deviations observed at higher pressures.

The proposed mathematical model combines passive hyperelasticity with active SMCs to simulate vascular behaviour. Using 3D-shell elements and incorporating the Ogden hyperelastic law for the passive component, the model captures nonlinear strain-stress relationships, enabling realistic simulations of arterial behaviour under varying dynamical conditions. The model integrates an affine stress-strain constitutive law for SMC fibres with two parameters, the pre-stress, k_0 , and the elastic modulus of the fibres, k_1 , enabling the simulation of vasoconstriction and vasodilation. Through validation against experimental data, the model provides valuable insights into the mechanical dynamics of SMC contraction, offering a promising approach for understanding vascular function and exploring the simulation of *in vivo* data.

Although structure-based passive mechanical models of blood vessels have been studied extensively (Lanir, 1983; Wuyts et al, 1995; Dahl et al, 2008; Lokshin and Lanir, 2009; Hollander et al, 2011; Rachev and Shazly, 2019), there remains a notable gap in the development of models addressing active properties. Mechanical studies of active vessels have predominantly relied on phenomenological models, primarily due to the complex micro-environment of SMCs and the coupled mechanical and chemical kinetics (Gestrelus and Borgström, 1986; Yang et al, 2003a; Stålhand et al, 2011). The majority of the active blood vessel constitutive models suggest uniaxial length-tension relationships in the circumferential direction as motivated by the circumferential arrangement of SMCs (Clark and Glagov, 1985; Wolinsky and Glagov, 1967; Hansen et al, 1980; O’Connell et al, 2008).

The choice between 0D, 1D, 2D, or 3D models is influenced by the level of spatial detail required and the complexity of the phenomena under investigation. 1D models are usually validated against *in vitro* (Westerhof et al, 1971) and they present a higher computational efficiency in comparison to 3D models. However, with low-dimensional models it is not possible to account for the detailed structural features of the wall, such as nonlinearity, anisotropy, and residual stresses while 3D structural models become essential when detailed spatial information is necessary to capture complex vessel geometries and interactions. The majority of models concerning SMCs rely on either 0D ordinary differential equations or 1D formulations (Rachev and Hayashi, 1999; Fay and Delise, 1973; Lee and Schmid-Schönbein, 1996; Yang et al, 2003a,b; Bursztyn et al, 2007; Murtada et al, 2010; Jin et al, 2020). For instance, Jin et al (2020) used a 1D model to simulate arterial blood pressure, blood flow, wall shear stress, and luminal diameter during flow-mediated dilation tests, employing principles of mass and momentum conservation alongside an elastic tube law for pressure changes is developed. Coccarelli et al (2021) and Liu (2014) focused on characterising the biomechanical features of SMC contractility, whilst Chen et al (2013) introduced a

structural passive model alongside a 2D active vascular smooth muscle model capable of predicting axial vasoactivity. Furthermore, [Murtada et al \(2012\)](#) implemented Hill's three-element model coupled with the four-state latch model by Hai and Murphy to capture electromechanical activation in the pig carotid media, successfully predicting isometric contraction, sudden extensions, and length-tension relationships.

In general, there is a lack of studies modelling SMC activation within the continuum mechanics framework. For example, Stålhand and co-authors based on their one-dimensional model (see [Stålhand et al \(2008\)](#)), developed in [Stålhand et al \(2011\)](#) a mechanochemical 3D continuum model for SMC contraction. However, although the model has been developed in a 3D continuum framework, uniaxial examples have been shown, only. [Coccarelli et al \(2018\)](#) introduces a 3D derived, fibre-reinforced, hyperelastic structural model, coupled with an axisymmetric, reduced-order model for blood flow. This model incorporates the relationship between vessel transmural pressure and lumen area via a Holzapfel–Ogden type law, while also considering residual stresses along the vessel's thickness and length. Despite the increased complexity and parameter count compared to standard pressure-area tube laws, the advantages of employing such a model are numerous. Firstly, it can account for various conditions and pharmacological agent effects, such as axial loading, fibre dispersion, residual stress, and potentially active contractility. Secondly, the structural model developed by Holzapfel and colleagues that is used in [Coccarelli et al \(2018\)](#) captures the non-linear behaviour of vascular tissue, especially under blood pressure loads significantly above the physiological range.

In our study, the 3D structural model proposed shares some similarities from the other 3D models proposed but also brings new contributions. Our model integrates a 3D hyperelastic law for the passive component, strengthened by active fibres. Unlike the approach in [Coccarelli et al \(2018\)](#) or [Stålhand et al \(2011\)](#), we have not included the chemical driving mechanism. However, we have employed 3D-shell finite elements

to avoid numerical locking and manage large displacements, as evidenced in dynamic simulations. In contrast to [Coccarelli et al \(2018\)](#), which performs the model validation through isometric tests, our model is validated as well through uniaxial static tests with biaxial deformation measurements and uniaxial dynamical ones. In general, with this type of models we could incorporate them in *in vivo* more complex geometries and be able to describe a full haemodynamic model.

One of the interests of the present study is to determine whether the contraction of SMCs directly affects vascular tone by regulating stiffness through the fibres. Additionally, it is aimed to understand whether this regulation indirectly adjusts intrinsic stiffness, as indicated by changes in the Young modulus. Furthermore, the investigation explores the extent of alterations in geometry, such as changes in diameter, influence biomechanical assessments. Taking a look at how the pre-stress k_0 and elastic modulus k_1 of the fibres change compared to the baseline conditions gives us more understanding about the regulation of vascular tone. For vasoconstrictors, there is an increase in pre-stress, reflecting increased arterial tension and reduced compliance. Conversely, the response to DEANO exhibits a more subtle variation, with pre-stress showing variable changes, influenced by the complex interplay of vasodilation and previously vasoconstriction compensatory mechanisms. Similarly, the elastic modulus exhibits distinct trends, vasoconstrictors tend to increase vessel stiffness, while vasodilators often lead to a decrease or maintenance of elasticity, highlighting the dynamic nature of vascular responses to vasoactive compounds. In addition to the observed changes in pre-stress and elastic modulus of the active fibres, it is remarkable that the parameters associated with the passive component of the arterial wall, such as Young's modulus and thickness, exhibit minimal variation across conditions. The fact that there was no notable change, suggests that alterations in arterial mechanics primarily stem from the active component governed by SMC activity rather than intrinsic vessel properties.

The Young's modulus staying comparatively stable indicates that the intrinsic stiffness of the vessel, represented by the passive component, remains largely unchanged. Instead, the variations in k_0 and k_1 point towards the crucial role of SMCs in mediating vasoconstriction and dilation, with minimal contribution from changes in intrinsic stiffness.

The simulated arterial stiffness values demonstrate a consistent decrement at higher pressures across all examined conditions in comparison to experimental values, necessitating a re-estimation. This observed discrepancy may potentially stem from the inherent limitations of the current model, which does not account for the recruitment of stiffer collagen fibres situated in the adventitial layer. These fibres are known to be recruited in a pressure-dependent manner within the aorta. Consequently, the model's omission of collagen loading contributes to an underestimation of stiffness values at highest pressures.

Overall, our work introduces a new mathematical model to explore arterial mechanics, shedding light on the roles of SMCs. Moving forward, future research could focus on refining and validating the model to better capture the complex dynamics of arterial mechanics. This includes addressing limitations such as the lack of consideration for collagen loading, which may influence parameter estimation accuracy, particularly at higher pressures. As future work we would like to incorporate a more sophisticated model with a realistic geometry that also accounts for the contact between the aortic segment and the hooks, providing a more comprehensive understanding of vascular mechanics and interactions. Moreover, the application of the model to *in vivo* data holds promising prospects for advancing our understanding of vascular physiology and guiding the development of further experiments. By integrating experimental findings and clinical data, the model can contribute to more accurate predictions of vascular behaviour under physiological and pathological conditions.

Acknowledgments. SC and CW are ESR-fellows of the INSPIRE European Training Network (Guns et al, 2020). INSPIRE receives funding from the EU Horizon 2020 Research and Innovation programme, under the Marie Skłodowska-Curie GA 858070.

Author contributions. CW collected the data. CW and PJ assisted the data analysis from a biological viewpoint. SC developed the mathematical model, its implementation and the parameter estimation. MV, MF and DL contributed to mathematical model and parameter estimation definition.

All authors contributed to the manuscript. CW and SC prepared the figures and the result analysis and post-processing.

Declarations

Competing interests. The authors declare no competing interests.

Ethical approval. The research conducted adhered to the standards outlined in the Guide for the Care and Use of Laboratory Animals, as issued by the US National Institutes of Health (NIH Publication No. 85-23, revised 1996), and all experimental procedures were in compliance with Directive 2010/63/EU of The European Parliament and The Council regarding the protection of animals used for scientific purposes. Furthermore, per the Belgium Royal Decree of May 2013, harvesting of organs for *ex vivo* analysis is not considered an animal experiment and therefore is exempt from ethical approval.

Appendix A Experimental data

We have used **isometric data** gathered from 9 aortic segments that have been contracted with PE by adding cumulative concentrations and after dilated with DEANO with a similar protocol.

Regarding the **ROTSAC experiments**, we have used data from other 15 segments divided in four sets of five, two, two and six segments, respectively. The ROTSAC data are presented in Table A1.

Pressures (mmHg)	Sets	KR	PE	5HT	50K	DEANO
60 - 100	Set 4: 6 segments	✓	✓			✓
80 - 120	Set 1: 5 segments	✓	✓			
	Set 2: 2 segments	✓		✓		
	Set 3: 2 segments	✓			✓	
	Set 4: 6 segments	✓	✓			✓
100 - 140	Set 4: 6 segments	✓	✓			✓
120 - 160	Set 4: 6 segments	✓	✓			✓

Table A1: ROTSAC data of 15 aortic segments where KR stands for Krebs-Ringer; PE, 5HT and 50K are the vasoconstrictors; DEANO is the vasodilator

Appendix B Ogden's constitutive law

The simplest hyperelastic material model is the Saint-Venant-Kirchhoff model, which is just an extension of the geometrically linear elastic material model to the geometrically nonlinear regime.

The strain energy density function for the Saint-Venant-Kirchhoff model is

$$W(\mathbf{e}) = \frac{\lambda}{2}(\text{tr}(\mathbf{e}))^2 + \mu \text{tr}(\mathbf{e}^2). \quad (\text{B1})$$

Equation (B1) can be written in terms of the invariants of \mathbf{C} as

$$W = \left(\frac{\lambda}{8} + \frac{\mu}{4}\right) I_1^2 - \frac{\mu}{2} I_2 - \left(\frac{3\lambda}{4} + \frac{\mu}{2}\right) I_1 + \frac{9\lambda}{8} + \frac{3\mu}{4},$$

where λ is the first Lamé parameter and μ is the shear modulus or the second Lamé parameter, given by

$$\lambda = \frac{\nu E}{(1 + \nu)(1 - 2\nu)}, \quad \mu = \frac{E}{2(1 + \nu)},$$

being E the Young modulus and ν the Poisson's ratio.

The Saint-Venant Kirchhoff constitutive law is well-suited for materials with small deformations and linear stress-strain behaviour. However, in scenarios involving large deformations and non-linear stress-strain responses, such as those often encountered in biological tissues, this model may not offer accurate representations.

To capture more complex behaviours, the Ogden constitutive law proves to be a better option for describing the passive component of the elastic medium. Ogden's model accommodates large deformations and non-linear material responses, thereby providing a more accurate representation of the behaviour seen in complex materials like rubbers, polymers, and biological tissues.

In terms of the invariants of \mathbf{C} , the Ogden's constitutive law ([Geymonat and Ciarlet, 1982](#)) can be written as

$$W = c_1(I_1 - 3) + c_2(I_2 - 3) + a(I_3 - 1) - (c_1 + 2c_2 + a) \ln(I_3),$$

with c_1, c_2 and a being the material parameters.

Interest lies in establishing a relation between the Ogden parameters and the Lamé parameters. The asymptotic behaviour of the Ogden law is examined as $|\mathbf{e}| \rightarrow 0$, aiming to identify it with the Saint-Venant-Kirchhoff law ([B1](#)). Upon conducting a limit development up to second order in \mathbf{e} , it can be demonstrated (refer to the detailed computation in [Trabelsi \(2004\)](#); [Ciarlet \(1988\)](#)).

$$\begin{cases} 2c_1 + 2c_2 = \mu, \\ c_2 + a = \frac{\lambda}{4}, \\ \lambda + 2\mu = 2b, \\ b = 2c_1 + 4c_2 + 2a. \end{cases}$$

Usually c_2 can be chosen such that $c_2 = c_1/\kappa$, with $\kappa \in [2, 100]$. After doing some algebra, it is possible to write

$$\begin{cases} c_1 = \frac{E}{4(1+\nu)(1+\frac{1}{\kappa})}, \\ c_2 = \frac{c_1}{\kappa}, \\ a = \frac{\nu E}{4(1+\nu)(1-2\nu)} - \frac{c_1}{\kappa}. \end{cases}$$

Appendix C 3D-shell elements

The Green-Lagrange tensor, in local coordinates (r, s, z) , writes:

$$e_{ij}(\vec{U}) := \frac{1}{2}(\vec{g}_i \cdot \vec{U}_{,j} + \vec{g}_j \cdot \vec{U}_{,i} + \vec{U}_{,i} \cdot \vec{U}_{,j}), \quad (\text{C2})$$

where \vec{g}_i is a covariant basis.

The first and second order infinitesimal variations are given by

$$\begin{aligned} \delta e_{ij} &:= \frac{1}{2}(\vec{g}_i \cdot \delta \vec{U}_{,j} + \vec{g}_j \cdot \delta \vec{U}_{,i} + \vec{U}_{,i} \cdot \delta \vec{U}_{,j} + \vec{U}_{,j} \cdot \delta \vec{U}_{,i}), \\ d\delta e_{ij} &:= \frac{1}{2}(d\vec{U}_{,i} \cdot \delta \vec{U}_{,j} + d\vec{U}_{,j} \cdot \delta \vec{U}_{,i}), \end{aligned}$$

The Green-Lagrange tensor is a nonlinear function of \vec{U} , the state variable of the problem. Newton's algorithm is selected for this purpose.

At each time of the backward Euler time-discretisation, a nonlinear problem has to be solved. The bilinear form appearing in this algorithm is the following:

$$A = A^L + A^{NL},$$

with

$$A^L(d\vec{U}, \delta\vec{U}) := \int_{\Omega} \frac{\partial^2 W}{\partial e_{ij} \partial e_{kl}} de_{kl} \delta e_{ij} dV,$$

$$A^{NL}(d\vec{U}, \delta\vec{U}) := \int_{\Omega} \frac{\partial W}{\partial e_{ij}} d\delta e_{ij} dV,$$

and the corresponding nonlinear right-hand side

$$F^{NL} := \int_{\Omega} \frac{\partial W}{\partial e_{ij}} \delta e_{ij} dV.$$

Appendix D Isometric tests

In this appendix, more detailed results of the estimation of the range of the pre-stress from the isometric data are presented. In Figure D1, the fitting of the measured forces to equation (10) is shown.

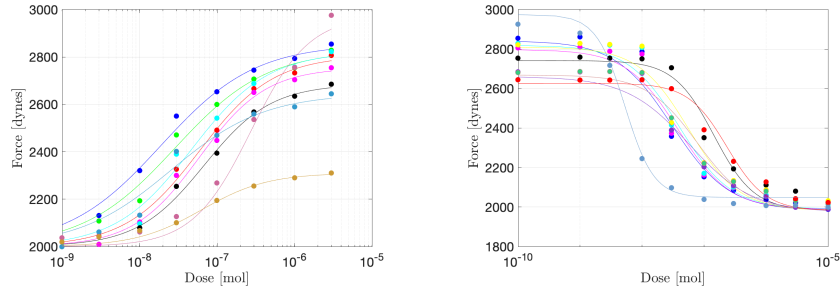


Fig. D1: Fitting of F_m to equation (10) for PE (left) and for DEANO (right) in semilog scale

The fitting of the data of the active pre-stress to equation (D2) is presented in Figure D2. Looking at the values at a concentration of 2 μM , is possible to do an estimation of the range of k_0 .

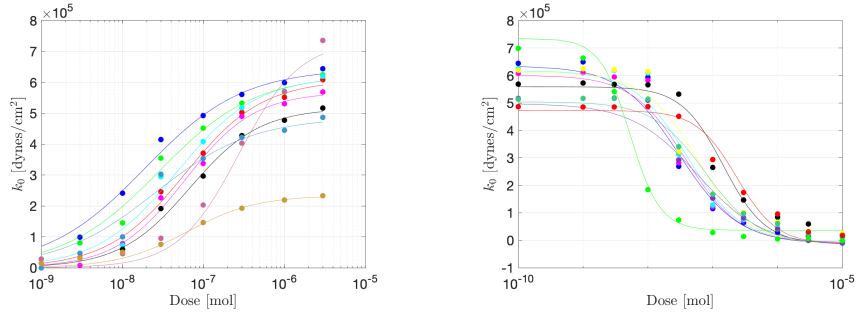


Fig. D2: k_0 for PE (left) and for DEANO (right) in semilog scale

Appendix E Optimization algorithm

To obtain the parameters for each aortic segment, a Control Random Research (CRS) algorithm is used for optimisation (Price, 1978). The optimisation problem is formulated in (6). A point θ_{opt} is considered a global minimiser of J if $J_{opt} = J(\theta_{opt}) \leq J(\theta)$ for all $\theta \in \mathcal{W}$.

CRS algorithms are better in high-dimensional problems compared to DIRECT algorithms. Unlike gradient-based methods, CRS algorithms do not use properties of the function being optimised. The only requirements are that $J(\theta)$ can be computed for any $\theta \in \mathcal{W}$, and the explicit expression of the function being optimised must be known.

In each step of the algorithm, $n + 1$ points are randomly chosen to create a simplex in n -dimensional space. One of these points becomes the pole, and the next trial point is determined by reflecting this pole relative to the centroid of the remaining points. This process generates primary trial points for exploration and secondary trial points for convergence, with the choice between them depending on the algorithm's success rate. If the success rate is below 50%, and a primary trial fails, a secondary point is selected for the next trial, maintaining a balanced approach between exploration and convergence during optimisation.

In summary, the CRS algorithm is a heuristic, direct search method that begins by populating a set S with a large sample ($N \gg n$) distributed uniformly over the search space \mathbf{W} . This sample is gradually contracted by replacing the worst point in S with a better trial point, forming a simplex with $n + 1$ randomly chosen points from S . This process continues until a specified stopping condition is met.

The main issues with CRS are its lack of robustness in locating the global minimum and its decreased efficiency in convergence, particularly after reaching the region of the global minimum. To enhance the robustness and efficiency of CRS, Kaelo and Ali proposed variants such as CRS2, suggesting modifications to the trial point generation schemes (Price, 1983). Specifically, a CRS algorithm with local mutation for optimisation is chosen (Kaelo and Ali, 2006).

In the original algorithm, if a trial point fails to improve upon the current worst point in the sample S , it is discarded, and a new simplex is formed using a new set of $n + 1$ points from S .

In CRS with local mutation, the unsuccessful trial point is not discarded but used to obtain a second trial point. The point generation scheme is modified by introducing a local mutation technique. Whenever a trial point generated in CRS fails to replace the current worst point in S , local mutation generates a second trial point exploring the region around the current best point in S by reflecting the trial point through the current best point. This modification is utilised whenever a trial point fails to yield a function value that can replace the current worst point in S .

The introduction of local mutation has enhanced these algorithms' robustness in finding the global minimum and efficiency in reducing the number of function evaluations and CPU time. Additionally, the local mutation technique expedites convergence as soon as the region of the global minimiser is reached.

References

- Aletti M, Gerbeau JF, Lombardi D (2015) Modeling autoregulation in three-dimensional simulations of retinal hemodynamics. *Modeling and Artificial Intelligence in Ophthalmology* 1:12. <https://doi.org/10.35119/maio.v1i1.17>
- Ambrosi D, Pezzuto S (2012) Active stress vs. active strain in mechanobiology: Constitutive issues. *Journal of Elasticity* 107:199–212. <https://doi.org/10.1007/s10659-011-9351-4>
- Bit A, Suri JS, Ranjani A (2020) *Anatomy and physiology of blood vessels*. IOP Publishing, <https://doi.org/10.1088/978-0-7503-2088-7ch1>
- Bursztyn L, Eytan O, Jaffa A, et al (2007) Mathematical model of excitation–contraction in a uterine smooth muscle cell. *American Journal of Physiology: Cell Physiology* 292(5):C1816–C1829. <https://doi.org/10.1152/ajpcell.00478.2006>
- Chapelle D, Bathe KJ (2010) *The Finite Element Analysis of Shells - Fundamentals*. Springer-Verlag
- Chapelle D, Ferent A, Bathe KJ (2004) 3D-shell elements and their underlying mathematical model. *Math Models Methods Appl Sci* 14(1):105–142. <https://doi.org/10.1142/S0218202504003179>
- Chen H, Luo T, Zhao X, et al (2013) Microstructural constitutive model of active coronary media. *Biomaterials* 34(31):7575–7583. <https://doi.org/10.1016/j.biomaterials.2013.06.035>
- Ciarlet PG (1988) Chapter 4: Hyperelasticity. In: Ciarlet PG (ed) *Mathematical Elasticity Volume I: Three-Dimensional Elasticity, Studies in Mathematics and Its Applications*, vol 20. p 137–198, [https://doi.org/10.1016/S0168-2024\(08\)70061-4](https://doi.org/10.1016/S0168-2024(08)70061-4)

- Clark JM, Glagov S (1985) Transmural organization of the arterial media. the lamellar unit revisited. *Arteriosclerosis* 5:19–34. <https://doi.org/10.1161/01.ATV.5.1.19>
- Coccarelli A, Edwards DH, Aggarwal A, et al (2018) A multiscale active structural model of the arterial wall accounting for smooth muscle dynamics. *J R Soc Interface* 15(139):20170732. <https://doi.org/10.1098/rsif.2017.0732>
- Coccarelli A, Carson JM, Aggarwal A, et al (2021) A framework for incorporating 3d hyperelastic vascular wall models in 1d blood flow simulations. *Biomech Model Mechanobiol* 20(4):1231–1249. <https://doi.org/10.1007/s10237-021-01437-5>
- Dahl SLM, Vaughn ME, Hu JJ, et al (2008) A microstructurally motivated model of the mechanical behavior of tissue engineered blood vessels. *Ann Biomed Eng* 36:1782–1792. <https://doi.org/10.1007/s10439-008-9554-4>
- De Moudt S, Hendrickx J, Neutel C, et al (2022a) Aortic stiffness in l-name treated c57bl/6 mice displays a shift from early endothelial dysfunction to late-term vascular smooth muscle cell dysfunction. *Frontiers in Physiology* 13:874015. <https://doi.org/10.3389/fphys.2022.874015>
- De Moudt S, Hendrickx JO, Neutel C, et al (2022b) Progressive aortic stiffness in aging c57bl/6 mice displays altered contractile behaviour and extracellular matrix changes. *Communications Biology* 5(1):605. <https://doi.org/10.1038/s42003-022-03563-x>
- Decoene A, Martin S, Vergnet F (2023) A continuum active structure model for the interaction of cilia with a viscous fluid. *Journal of Applied Mathematics and Mechanics / Zeitschrift für Angewandte Mathematik und Mechanik* <https://doi.org/10.1002/zamm.202100534>

- Fay F, Delise C (1973) Contraction of isolated smooth-muscle cells—structural changes. *Proceedings of the National Academy of Sciences of the United States of America* 70(3):641–645. <https://doi.org/10.1073/pnas.70.3.641>
- Gestrelus S, Borgström P (1986) A dynamic model of smooth muscle contraction. *Biophys J* 50:157–169. [https://doi.org/10.1016/S0006-3495\(86\)83448-8](https://doi.org/10.1016/S0006-3495(86)83448-8)
- Geymonat G, Ciarlet PG (1982) Sur les lois de comportement en élasticité non linéaire compressible. *CR Acad Sci Paris Sér II* 295:423–426
- Ghosh A, Dharmarajan A, Swain PK, et al (2019) Impact of cardiovascular factors on pulse wave velocity and total vascular resistance in different age group patients with cardiovascular disorders. *Curr Aging Sci* 11(4):261–268. <https://doi.org/10.2174/1874609812666190226151500>
- Guns PD, Guth BD, Braam S, et al (2020) Inspire: A european training network to foster research and training in cardiovascular safety pharmacology. *Journal of Pharmacological and Toxicological Methods* 105:106889. <https://doi.org/10.1016/j.vascn.2020.106889>
- Hansen TR, Dineen DX, Pullen GL (1980) Orientation of arterial smooth muscle and strength of contraction of aortic strips from doca-hypertensive rats. *Blood Vessels* 17:302–311. <https://doi.org/10.1159/000158261>
- Hollander Y, Durban D, Lu X, et al (2011) Experimentally validated microstructural 3d constitutive model of coronary arterial media. *J Biomech Eng* 133:031007. <https://doi.org/10.1115/1.4003324>
- Jin W, Chowienczyk P, Alastruey J (2020) An in silico simulation of flow-mediated dilation reveals that blood pressure and other factors may influence the response

- independent of endothelial function. *Am J Physiol Heart Circ Physiol* 318(5):H1337–H1345. <https://doi.org/10.1152/ajpheart.00703.2019>
- Johnson SG (2014) The nlopt nonlinear-optimization package, <http://github.com/stevengj/nlopt>
- Kaelo P, Ali MM (2006) Some variants of the controlled random search algorithm for global optimization. *Journal of Optimization Theory and Applications* 130(2):253–264. <https://doi.org/10.1007/s10957-006-9101-0>
- Kerage D, Brindley DN, Hemmings DG (2014) Review: novel insights into the regulation of vascular tone by sphingosine 1-phosphate. *Placenta* 35:S86–S92. <https://doi.org/10.1016/j.placenta.2013.12.006>
- Lacolley P, Regnault V, Segers P, et al (2017) Vascular smooth muscle cells and arterial stiffening: Relevance in development, aging, and disease. *Physiol Rev* 97(4):1555–1617. <https://doi.org/10.1152/physrev.00003.2017>
- Lanir Y (1983) Constitutive equations for fibrous connective tissues. *J Biomech* 16:1–12. [https://doi.org/10.1016/0021-9290\(83\)90041-6](https://doi.org/10.1016/0021-9290(83)90041-6)
- Lee S, Schmid-Schönbein G (1996) Biomechanical model for the myogenic response in the microcirculation. Part 1 - - formulation and initial testing. *Journal of Biomechanical Engineering* 118(2):145–151. <https://doi.org/10.1115/1.2795952>
- Leloup AJA, Van Hove CE, Kurdi A, et al (2016) A novel set-up for the ex vivo analysis of mechanical properties of mouse aortic segments stretched at physiological pressure and frequency. *J Physiol* 594(21):6105–6115. <https://doi.org/10.1113/JP272623>
- Leloup AJA, Van Hove CE, De Moudt S, et al (2019) Vascular smooth muscle cell contraction and relaxation in the isolated aorta: a critical regulator of large artery

- compliance. *Physiol Rep* 7(4):e13934. <https://doi.org/10.14814/phy2.13934>
- Libai A, Simmonds J (2005) *The nonlinear theory of elastic shells*. Cambridge University Press
- Liu T (2014) A constitutive model for cytoskeletal contractility of smooth muscle cells. *Proc R Soc A* 470(20130771). <https://doi.org/10.1098/rspa.2013.0771>
- Lohr MJ, Sugerman GP, Kakaletsis S, et al (2022) An introduction to the ogden model in biomechanics: benefits, implementation tools and limitations. *Philos Trans A Math Phys Eng Sci* 380:20210365. <https://doi.org/10.1098/rsta.2021.0365>
- Lokshin O, Lanir Y (2009) Micro and macro rheology of planar tissues. *Biomaterials* 30:3118–3127. <https://doi.org/10.1016/j.biomaterials.2009.02.039>
- Murtada S, Kroon M, Holzapfel G (2010) A calcium-driven mechanochemical model for prediction of force generation in smooth muscle. *Biomechanics and Modelling in Mechanobiology* 9(6):749–762. <https://doi.org/10.1007/s10237-010-0211-0>
- Murtada SC, Arner A, Holzapfel GA (2012) Experiments and mechanochemical modeling of smooth muscle contraction: significance of filament overlap. *J Theor Biol* 297:176–186. <https://doi.org/10.1016/j.jtbi.2011.11.012>
- Murtada SI, Holzapfel GA (2014) Investigating the role of smooth muscle cells in large elastic arteries: a finite element analysis. *J Theor Biol* 358:1–10. <https://doi.org/10.1016/j.jtbi.2014.04.028>
- Nedrelov DS, Townsend JM, Detamore MS (2023) The ogden model for hydrogels in tissue engineering: Modulus determination with compression to failure. *Journal of Biomechanics* 152:111592. <https://doi.org/10.1016/j.jbiomech.2023.111592>

- O'Connell MK, Murthy S, Phan S, et al (2008) The three-dimensional micro- and nanostructure of the aortic medial lamellar unit measured using 3d confocal and electron microscopy imaging. *Matrix Biol* 27:171–181. <https://doi.org/0.1016/j.matbio.2007.10.008>
- Price WL (1978) A controlled random search procedure for global optimization. *Toward Global Optimization* 2 pp 71–84
- Price WL (1983) Global optimization by controlled random search. *Journal of Optimization Theory and Applications* 40:333–348
- Rachev A, Hayashi K (1999) Theoretical study of the effects of vascular smooth muscle contraction on strain and stress distributions in arteries. *Annals of Biomedical Engineering* 27(4):459–468. <https://doi.org/10.1114/1.191>
- Rachev A, Shazly T (2019) A structure-based constitutive model of arterial tissue considering individual natural configurations of elastin and collagen. *J Mech Behav Biomed Mater* 90:61–72. <https://doi.org/10.1016/j.jmbbm.2018.09.047>
- Sahani AK, Shah MI, Radhakrishnan R, et al (2016) An imageless ultrasound device to measure local and regional arterial stiffness. *IEEE Trans Biomed Circuits Syst* 10(1):200–208. <https://doi.org/10.1109/TBCAS.2015.2394468>
- Sehgel NL, Zhu Y, Sun Z, et al (2013) Increased vascular smooth muscle cell stiffness: a novel mechanism for aortic stiffness in hypertension. *Am J Physiol Heart Circ Physiol* 305(9):H1281–H1287. <https://doi.org/10.1152/ajpheart.00232.2013>
- Sharif S, Visseren FLJ, Spiering W, et al (2019) Arterial stiffness as a risk factor for cardiovascular events and all-cause mortality in people with type 2 diabetes. *Diabet Med* 36(9):1125–1132. <https://doi.org/10.1111/dme.13954>

- Shirwany NA, Zou MH (2010) Arterial stiffness: a brief review. *Acta Pharmacol Sin* 31(10):1267–1276. <https://doi.org/10.1038/aps.2010.123>
- Stålhand J, Klarbring A, Holzapfel G (2008) Smooth muscle contraction: mechanochemical formulation for homogeneous finite strains. *Progress in Biophysics and Molecular Biology* 96(1-3):465–481. <https://doi.org/10.1016/j.pbiomolbio.2007.07.025>
- Stålhand J, Klarbring A, Holzapfel GA (2011) A mechanochemical 3d continuum model for smooth muscle contraction under finite strains. *J Theor Biol* 268:120–130. <https://doi.org/10.1016/j.jtbi.2010.10.013>
- Thomas B, Sumam KS (2016) Blood flow in human arterial system-a review. *Procedia Technology* 24:339–346. <https://doi.org/10.1016/j.protcy.2016.05.045>
- Trabelsi K (2004) On the modeling of thin plates in nonlinear elasticity. PhD thesis, Université Pierre et Marie Curie-Paris VI
- Vlachopoulos C (2010) Prediction of cardiovascular events and all-cause mortality with arterial stiffness: a systematic review and meta-analysis. *J Am Coll Cardiol* 55(12):1318–1327. <https://doi.org/10.1016/j.jacc.2009.10.061>
- Wang M, Monticone RE, Lakatta EG (2016) Chapter 13 - the aging arterial wall. In: Kaeberlein MR, Martin GM (eds) *Handbook of the Biology of Aging* (Eighth Edition). Academic Press, p 359–389, <https://doi.org/10.1016/B978-0-12-411596-5.00013-7>
- Westerhof N, Elzinga G, Sipkema P (1971) An artificial arterial system for pumping hearts. *J Appl Physiol* 31(5):776–81. <https://doi.org/10.1152/jappl.1971.31.5.776>

- Wolinsky H, Glagov S (1967) A lamellar unit of aortic medial structure and function in mammals. *Circ Res* 20:99–111. <https://doi.org/10.1161/01.res.20.1.99>
- Wuyts FL, Vanhuyse VJ, Langewouters GJ, et al (1995) Elastic properties of human aortas in relation to age and atherosclerosis: a structural model. *Phys Med Biol* 40:1577–1597. <https://doi.org/10.1088/0031-9155/40/10/002>
- Yang J, Clark J, Bryan R, et al (2003a) The myogenic response in isolated rat cerebrovascular arteries: smooth muscle cell model. *Medical Engineering & Physics* 25(8):691–709. [https://doi.org/10.1016/s1350-4533\(03\)00100-0](https://doi.org/10.1016/s1350-4533(03)00100-0)
- Yang J, Clark J, Bryan R, et al (2003b) The myogenic response in isolated rat cerebrovascular arteries: vessel model. *Medical Engineering & Physics* 25(8):711–717. [https://doi.org/10.1016/s1350-4533\(03\)00101-2](https://doi.org/10.1016/s1350-4533(03)00101-2)
- Yosibash Z, Priel E (2012) Artery active mechanical response: High order finite element implementation and investigation. *Computer Methods in Applied Mechanics and Engineering* 237-240:51–66. <https://doi.org/10.1016/j.cma.2012.05.001>
- Zhang Y, Agnoletti D, Xu Y, et al (2014) Carotid-femoral pulse wave velocity in the elderly. *J Hypertens* 32(8):1572–1576. <https://doi.org/10.1097/HJH.000000000000187>